PHYSICAL REVIEW A **81**, 042113 (2010)

Geometric phase in entangled systems: A single-neutron interferometer experiment

S. Sponar,[1,*] J. Klepp,[1] R. Loidl,[1] S. Filipp,[2] K. Durstberger-Rennhofer,[1] R. A. Bertlmann,[3] G. Badurek,[1]
H. Rauch,[1,4] and Y. Hasegawa[1]

[1]*Atominstitut der Österreichischen Universitäten, A-1020 Vienna, Austria*
[2]*Department of Physics, Eidgenössische Technische Hochschule Zürich, Schafmattstrasse 16, CH-8093 Zurich, Switzerland*
[3]*Faculty of Physics, University of Vienna, Boltzmanngasse 5, A-1090 Vienna, Austria*
[4]*Institut Laue-Langevin, Boîte Postale 156, F-38042 Grenoble CEDEX 9, France*

(Received 28 July 2009; published 30 April 2010)

The influence of the geometric phase on a Bell measurement, as proposed by Bertlmann *et al.* [Phys. Rev. A **69**, 032112 (2004)] and expressed by the Clauser-Horne-Shimony-Holt (CHSH) inequality, has been observed for a spin-path-entangled neutron state in an interferometric setup. It is experimentally demonstrated that the effect of geometric phase can be balanced by a change in Bell angles. The geometric phase is acquired during a time-dependent interaction with a radiofrequency field. Two schemes, polar and azimuthal adjustment of the Bell angles, are realized and analyzed in detail. The former scheme yields a sinusoidal oscillation of the correlation function S, dependent on the geometric phase, such that it varies in the range between 2 and $2\sqrt{2}$ and therefore always exceeds the boundary value 2 between quantum mechanic and noncontextual theories. The latter scheme results in a constant, maximal violation of the Bell-like CHSH inequality, where S remains $2\sqrt{2}$ for all settings of the geometric phase.

DOI: 10.1103/PhysRevA.81.042113 PACS number(s): 03.65.Vf, 03.75.Dg, 03.65.Ud, 07.60.Ly

I. INTRODUCTION

Since the famous 1935 Einstein-Podolsky-Rosen (EPR) gedanken experiment [1], much attention has been devoted to quantum entanglement [2], which is among the most striking peculiarities in quantum mechanics. In 1964, J. S. Bell [3] introduced inequalities for certain correlations which hold for the predictions of any hidden-variable theory applied [4]. However, a dedicated experiment was not feasible at the time. Five years later, Clauser, Horne, Shimony, and Holt (CHSH) reformulated Bell's inequality pertinent for the first practical test of the EPR claim [5]. Thereafter polarization measurements with correlated photon pairs [6], produced by atomic cascade [7,8] and parametric down-conversion of lasers [9–11], demonstrated a violation of the CHSH inequality. To this date, several systems [12–15] have been examined, including neutrons [16].

EPR experiments are designed to test local hidden-variable theories, thereby exploiting the concept of nonlocality. Local hidden-variable theories are a subset of a larger class of hidden-variable theories known as the noncontextual hidden-variable theories. Noncontextuality implies that the value of a measurement is independent of the experimental context, that is, of previous or simultaneous measurements [17,18]. Noncontextuality is a less stringent demand than locality because it requires mutual independence of the results for commuting observables even if there is no spacelike separation [19]. First tests of quantum contextuality, based on the Kochen-Specker theorem [20], have been recently proposed [21,22] and performed successfully using trapped ions [23] and neutrons [24,25].

In the case of neutrons, entanglement is not achieved between different particles but between different degrees of freedom. Since the observables of one Hilbert space commute with observables of a different Hilbert space, the single-neutron system is suitable for studying noncontextual hidden-variable theories. Using neutron interferometry [26,27], single-particle entanglement between the spinor and the spatial part of the neutron wave function [16] and full tomographic state analysis [28] have already been accomplished. In addition, creation of a triply entangled single-neutron state [29] by applying a coherent manipulation method of a neutron's energy degree of freedom has been demonstrated.

The total phase acquired during an evolution of a quantal system generally consists of two components: the usual dynamical phase $-1/\hbar \int H(t)dt$, which depends on the dynamical properties like energy or time, and a geometric phase γ, which is, considering a spin 1/2 system, minus half the solid angle $(\Omega/2)$ of the curve traced out in ray space. The peculiarity of this phase, first discovered by Berry in [30], lies in the fact that it does not depend on the dynamics of the system but purely on the evolution path of the state in parameter space. From its first verification, for photons in 1986 [31] and later for neutrons [32], generalizations such as nonadiabatic [33]; noncyclic [34], including the Pancharatnam relative phase [35]; off-diagonal evolutions [36–38]; and the mixed-state case [39–43] have been established.

The geometric phase in a single-particle system has been studied widely over the past two and a half decades. Nevertheless its effect on entangled quantum systems is less investigated. The geometric phase is an excellent candidate to be utilized for logic gate operations in quantum communication [44] because of its robustness against noise, which has been tested recently using superconducting qubits [45] and trapped polarized ultracold neutrons [46]. Entanglement is the basis for quantum communication and quantum information processing, and therefore studies on systems combing both quantum phenomena—the geometric phase and quantum entanglement—are of great importance [47–50].

---

[*] sponar@ati.ac.at

This article reports on an experimental confirmation for the violation of Bell-like inequality, relying on correlations between the spin and path degrees of freedom of a single-neutron system under the influence of the geometric phase. The geometric phase is generated in one of the complementary Hilbert spaces, in our case, the spin subspace. We demonstrate in detail how the geometric phase affects the Bell angle settings, required for a violation of a Bell-like inequality in the CHSH formalism, in a polarized neutron interferometric experiment. In Sec. II, the theoretical framework, as developed in [48], is briefly described for a spin-path-entangled neutron state. Expectation values and Bell-like inequalities are defined and the concepts of polar and azimuthal angle adjustment are introduced. Section III explains the actual measurement process. It focuses on experimental issues such as state preparation, manipulation of geometric phase, joint measurements, and the experimental strategy. In the principal part, data analysis and experimental results are presented. This is followed by Secs. IV and V, consisting of a discussion and a conclusion.

II. THEORY

A. Expectation values

First we want to clarify the notation since numerous angles are due to appear in this article. Angles denoted as $\boldsymbol{\alpha}$ are associated with path, and angles denoted as $\boldsymbol{\beta}$ with spin subspace. The prime symbol is used to distinguish different measurement directions of one subspace, required for a CHSH-Bell measurement [5] (e.g., $\boldsymbol{\alpha}$ and $\boldsymbol{\alpha}'$ represent the measurement directions for the path subspace). Index 1 denotes polar angles, whereas index 2 is identified with azimuthal angles (e.g., β_1 and β_1' are polar angles of the spin subspace). Finally, the $^\perp$ symbol is used for adding π to an angle (e.g., $\alpha_1^\perp = \alpha_1 + \pi$).

Following the notation given in [48], in our experiment, the neutron's wave function is defined in a tensor product of two Hilbert spaces: One Hilbert space is spanned by two possible paths in the interferometer given by $|\mathrm{I}\rangle, |\mathrm{II}\rangle$ and the other by spin-up and spin-down eigenstates, denoted as $|\Uparrow\rangle$ and $|\Downarrow\rangle$, referring to a quantization axis along a static magnetic field. Interacting with a time-dependent magnetic field, the entangled Bell state acquires a geometric phase γ tied to the evolution within the spin subspace [48]:

$$|\Psi_{\mathrm{Bell}}(\gamma)\rangle = \frac{1}{\sqrt{2}}(|\mathrm{I}\rangle \otimes |\Uparrow\rangle + |\mathrm{II}\rangle \otimes e^{i\gamma}|\Downarrow\rangle). \tag{1}$$

As in common Bell experiments, a joint measurement for spin and path is performed, thereby applying the projection operators for the path

$$\hat{P}^{\mathrm{p}}_{\pm}(\boldsymbol{\alpha}) = |\pm\boldsymbol{\alpha}\rangle\langle\pm\boldsymbol{\alpha}| \tag{2}$$

with

$$\begin{aligned} |+\boldsymbol{\alpha}\rangle &= \cos\frac{\alpha_1}{2}|\mathrm{I}\rangle + e^{i\alpha_2}\sin\frac{\alpha_1}{2}|\mathrm{II}\rangle, \\ |-\boldsymbol{\alpha}\rangle &= -\sin\frac{\alpha_1}{2}|\mathrm{I}\rangle + e^{i\alpha_2}\cos\frac{\alpha_1}{2}|\mathrm{II}\rangle, \end{aligned} \tag{3}$$

where α_1 denotes the polar angle and α_2 the azimuthal angle, and for the spin subspace,

$$\hat{P}^{s}_{\pm}(\boldsymbol{\beta}) = |\pm\boldsymbol{\beta}\rangle\langle\pm\boldsymbol{\beta}|, \tag{4}$$

with

$$\begin{aligned} |+\boldsymbol{\beta}\rangle &= \cos\frac{\beta_1}{2}|\Uparrow\rangle + e^{i\beta_2}\sin\frac{\beta_1}{2}|\Downarrow\rangle, \\ |-\boldsymbol{\beta}\rangle &= -\sin\frac{\beta_1}{2}|\Uparrow\rangle + e^{i\beta_2}\cos\frac{\beta_1}{2}|\Downarrow\rangle. \end{aligned} \tag{5}$$

Introducing the observables

$$\begin{aligned} \hat{A}^{\mathrm{p}}(\boldsymbol{\alpha}) &= \hat{P}^{\mathrm{p}}_{+}(\boldsymbol{\alpha}) - \hat{P}^{\mathrm{p}}_{-}(\boldsymbol{\alpha}), \\ \hat{B}^{\mathrm{s}}(\boldsymbol{\beta}) &= \hat{P}^{\mathrm{s}}_{+}(\boldsymbol{\beta}) - \hat{P}^{\mathrm{s}}_{-}(\boldsymbol{\beta}), \end{aligned} \tag{6}$$

one can define an expectation value for a joint measurement of spin and path along the directions $\boldsymbol{\alpha}$ and $\boldsymbol{\beta}$:

$$\begin{aligned} E(\boldsymbol{\alpha},\boldsymbol{\beta}) &= \langle\Psi|\hat{A}^{\mathrm{p}}(\boldsymbol{\alpha}) \otimes \hat{B}^{\mathrm{s}}(\boldsymbol{\beta})|\Psi\rangle \\ &= -\cos\alpha_1\cos\beta_1 - \cos(\alpha_2 - \beta_2 + \gamma)\sin\alpha_1\sin\beta_1 \\ &= -\cos(\alpha_1 - \beta_1) \text{ for } (\alpha_2 - \beta_2) = -\gamma. \end{aligned} \tag{7}$$

B. Bell-like inequalities

Next, a Bell-like inequality in a CHSH formalism [5] is introduced, consisting of four expectation values with the associated directions $\boldsymbol{\alpha}$, $\boldsymbol{\alpha}'$ and $\boldsymbol{\beta}$, $\boldsymbol{\beta}'$ for joint measurements of spin and path, respectively:

$$\begin{aligned} S(\boldsymbol{\alpha},\boldsymbol{\alpha}',\boldsymbol{\beta},\boldsymbol{\beta}',\gamma) &= |E(\boldsymbol{\alpha},\boldsymbol{\beta}) - E(\boldsymbol{\alpha},\boldsymbol{\beta}') + E(\boldsymbol{\alpha}',\boldsymbol{\beta}) + E(\boldsymbol{\alpha}',\boldsymbol{\beta}')| \\ &= |-\sin\alpha_1[\cos(\alpha_2 - \beta_2 - \gamma)\sin\beta_1 \\ &\quad - \cos(\alpha_2 - \beta_2' - \gamma)\sin\beta_1'] \\ &\quad - \cos\alpha_1(\cos\beta_1 - \cos\beta_1') \\ &\quad - \sin\alpha_1'[\cos(\alpha_2' - \beta_2 - \gamma)\sin\beta_1 \\ &\quad + \cos(\alpha_2' - \beta_2' - \gamma)\sin\beta_1'] \\ &\quad - \cos\alpha_1'(\cos\beta_1 + \cos\beta_1')|. \end{aligned} \tag{8}$$

The boundary of Eq. (8) is given by the value 2 for any noncontextual hidden-variable theories [51]. Without loss of generality, one angle can be eliminated by setting, for example, $\boldsymbol{\alpha} = 0$ ($\alpha_1 = \alpha_2 = 0$), which gives

$$\begin{aligned} S(\boldsymbol{\alpha}',\boldsymbol{\beta},\boldsymbol{\beta}',\gamma) &= |-\sin\alpha_1'[\cos(\alpha_2' - \beta_2 - \gamma)\sin\beta_1 \\ &\quad + \cos(\alpha_2' - \beta_2' - \gamma)\sin\beta_1'] - \cos\alpha_1' \\ &\quad \times (\cos\beta_1 + \cos\beta_1') - \cos\beta_1 + \cos\beta_1'|. \end{aligned} \tag{9}$$

Keeping the polar angles α_1', β_1, and β_1' constant at the usual Bell angles $\alpha_1' = \pi/2$, $\beta_1 = \pi/4$, and $\beta_1' = 3\pi/4$ (and azimuthal parts fixed at $\alpha_2' = \beta_2 = \beta_2' = 0$) reduces S to

$$S(\gamma) = |-\sqrt{2} - \sqrt{2}\cos\gamma|, \tag{10}$$

where the familiar maximum value of $2\sqrt{2}$ is reached for $\gamma = 0$. For $\gamma = \pi$, the value of S approaches zero.

1. *Polar angle adjustment*

Here we consider the case when the azimuthal angles are kept constant, for example, $\alpha_2' = \beta_2 = \beta_2' = 0$ ($\alpha_2 = 0$), denoted as

$$\begin{aligned} S(\alpha_1',\beta_1,\beta_1',\gamma) &= |-\sin\alpha_1'(\cos\gamma\sin\beta_1 + \cos\gamma\sin\beta_1') \\ &\quad - \cos\alpha_1'(\cos\beta_1 + \cos\beta_1') - \cos\beta_1 \\ &\quad + \cos\beta_1'|. \end{aligned} \tag{11}$$

The polar Bell angles β_1, β_1', and α_1' ($\alpha_1 = 0$), yielding a maximum S value, can be determined, with respect to the geometric phase γ, by calculating the partial derivatives (the extremum condition) of S in Eq. (11):

$$\frac{\partial S}{\partial \beta_1} = \sin\beta_1 + \cos\alpha_1' \sin\beta_1 - \cos\gamma \sin\alpha_1' \cos\beta_1 = 0,$$

$$\frac{\partial S}{\partial \beta_1'} = -\sin\beta_1' + \cos\alpha_1' \sin\beta_1' - \cos\gamma \sin\alpha_1' \cos\beta_1' = 0,$$

$$\begin{aligned}\frac{\partial S}{\partial \alpha_1'} &= \sin\alpha_1'(\cos\beta_1 + \cos\beta_1') \\ &\quad - \cos\gamma \cos\alpha_1'(\sin\beta_1 + \sin\beta_1') = 0. \end{aligned} \tag{12}$$

The solutions are given by

$$\beta_1 = \arctan(\cos\gamma), \tag{13a}$$

$$\beta_1' = \pi - \beta_1, \tag{13b}$$

$$\alpha_1' = \frac{\pi}{2}. \tag{13c}$$

With these angles, the maximal S decreases for $\gamma : 0 \to \pi/2$ and touches at $\gamma = \pi/2$ even the limit of the CHSH inequality $S = 2$.

2. *Azimuthal angle adjustment*

Next we discuss the situation where the standard maximal value $S = 2\sqrt{2}$ can be achieved by keeping the polar angles α_1', β_1, and β_1' constant at the Bell angles $\alpha_1' = \pi/2$, $\beta_1 = \pi/4$, and $\beta_1' = 3\pi/4$ ($\alpha_1 = 0$), while the azimuthal parts, α_2', β_2, and β_2' ($\alpha_2 = 0$), are varied. The corresponding S function is denoted as

$$\begin{aligned} S(\alpha_2', \beta_2, \beta_2', \gamma) = \Big| -\sqrt{2} - \frac{\sqrt{2}}{2}[\cos(\alpha_2' - \beta_2 - \gamma) \\ + \cos(\alpha_2' - \beta_2' - \gamma)]\Big|. \end{aligned} \tag{14}$$

The maximum value $2\sqrt{2}$ is reached for

$$\beta_2 = \beta_2', \tag{15a}$$

$$\alpha_2' - \beta_2' = \gamma (\mathrm{mod}\ \pi). \tag{15b}$$

For convenience, $\beta_2 = 0$ is chosen.

The conditions expressed in Eqs. (13a), (13b), and (15b) (see Bloch spheres in Fig. 1) are experimentally realized using the spin turner device and the neutron interferometer (IFM) depicted in Fig. 1.

III. DESCRIPTION OF THE EXPERIMENT

A. State preparation

The preparation of entanglement between spatial and spinor degrees of freedom is achieved by a beam splitter and a subsequent spin-flip process in one subbeam: Behind the beam splitter (first plate of the IFM), the neutron's wave function is found in a coherent superposition of $|\mathrm{I}\rangle$ and $|\mathrm{II}\rangle$, and only the spin in $|\mathrm{II}\rangle$ is flipped by the first radiofrequency (rf) flipper within the interferometer (see Fig. 1).

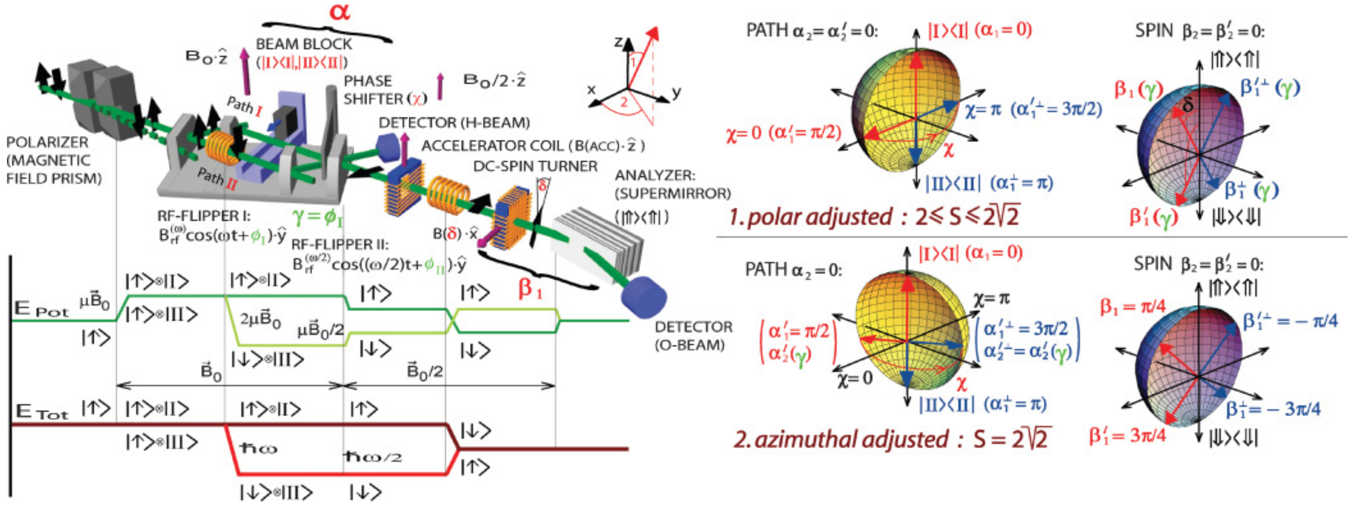

FIG. 1. (Color online) Experimental apparatus for joint measurement of spinor and path degrees of freedom with respect to the geometric phase. The incident neutron beam is polarized by a magnetic field prism. The spin state acquires a geometric phase γ during the interaction with a rf field within the interferometer. The second rf flipper compensates the energy difference between the two spin components because of its frequency of $\omega/2$, which is depicted in the energy level diagram of the two interfering subbeams. The accelerator coil is used to eliminate dynamic phase contributions. The beam block is required for measurements solely in one path ($\pm\hat{\mathbf{z}}$ direction of the path measurement). Finally, the spin is rotated by an angle δ (in the $\hat{\mathbf{x}}, \hat{\mathbf{z}}$ plane) by a dc-spin turner for a polarization analysis and count rate detection. The Bloch-sphere description includes the measurement settings of $\boldsymbol{\alpha}$ and $\boldsymbol{\beta}(\delta)$, determining the projection operators used for joint measurement of spin and path; $\boldsymbol{\alpha}$ is tuned by a combination of the phase shifter (χ) and the beam block, and $\boldsymbol{\beta}$ is adjusted by the angle δ.

The entangled state that emerges from a coherent superposition of $|\mathrm{I}\rangle$ and $|\mathrm{II}\rangle$ is expressed as

$$|\Psi_{\mathrm{Bell}}\rangle = \frac{1}{\sqrt{2}}(|\mathrm{I}\rangle \otimes |{\Uparrow}\rangle + |\mathrm{II}\rangle \otimes e^{i\omega t} e^{i\phi_{\mathrm{I}}}|{\Downarrow}\rangle), \tag{16}$$

after the interaction with the oscillating field, given by $B^{(1)} = B_{\mathrm{rf}}^{(\omega)} \cos(\omega t + \phi_{\mathrm{I}}) \cdot \hat{\mathbf{y}}$. The time-dependent phase ωt is due to the interaction with the time-dependent magnetic field, where the total energy of the neutron is no longer conserved [52–54] since photons of energy $\hbar\omega$ are exchanged with the rf field (for a more detailed description of the generation of $|\Psi_{\mathrm{Bell}}\rangle$, see [29]).

B. Manipulation of geometric and dynamical phases

The effect of the first rf flipper, placed inside the interferometer (path II), is described by the unitary operator $\hat{U}(\phi_{\mathrm{I}})$, which induces a spinor rotation from $|{\Uparrow}\rangle$ to $|{\Downarrow}\rangle$, denoted as $\hat{U}(\phi_{\mathrm{I}})|{\Uparrow}\rangle = e^{i\phi_{\mathrm{I}}}|{\Downarrow}\rangle$. The rotation axis encloses an angle ϕ_{I} with the $\hat{\mathbf{y}}$ direction and is determined by the oscillating magnetic field $B^{(1)} = B_{\mathrm{rf}}^{(\omega)} \cos(\omega t + \phi_{\mathrm{I}}) \cdot \hat{\mathbf{y}}$. Without loss of generality, one can insert a unity operator, given by $\mathbb{1} = \hat{U}^{\dagger}(\phi_0)\hat{U}(\phi_0)$, yielding

$$\begin{aligned} \hat{U}(\phi_{\mathrm{I}})|{\Uparrow}\rangle &= \overbrace{\hat{U}(\phi_{\mathrm{I}})\underbrace{\hat{U}^{\dagger}(\phi_0)}_{}}^{e^{i\gamma}}\underbrace{\,\hat{U}(\phi_0)}_{\mathbb{1}}|{\Uparrow}\rangle \\ &= e^{i\gamma}|{\Downarrow}\rangle, \end{aligned} \tag{17}$$

where $\hat{U}(\phi_0)$ can be interpreted as a rotation from $|{\Uparrow}\rangle$ to $|{\Downarrow}\rangle$, with the $\hat{\mathbf{y}}$ direction being the rotation axis ($\phi_0 = 0$), and $\hat{U}^{\dagger}(\phi_0)$ describes a rotation about the same axis back to the initial state $|{\Uparrow}\rangle$. Consequently, $\hat{U}(\phi_{\mathrm{I}})\hat{U}^{\dagger}(\phi_0)$ can be identified to induce the geometric phase γ along the reversed evolution path characterized by ϕ_0 ($|{\Downarrow}\rangle$ to $|{\Uparrow}\rangle$), followed by another path determined by ϕ_{I} ($|{\Uparrow}\rangle$ to $|{\Downarrow}\rangle$). In the rotating frame of reference [55], the two semigreat circles enclose an angle ϕ_{I} and the solid angle $\Omega = -2\phi_{\mathrm{I}}$, yielding a pure geometric phase

$$\gamma = -\Omega/2 = \phi_{\mathrm{I}}, \tag{18}$$

which is depicted in Fig. 2. The entangled state, as described in [48], is represented by

$$|\Psi_{\mathrm{Exp}}(\gamma)\rangle = \frac{1}{\sqrt{2}}(|\mathrm{I}\rangle \otimes |{\Uparrow}\rangle + |\mathrm{II}\rangle \otimes e^{i\omega t} e^{i\gamma}|{\Downarrow}\rangle), \tag{19}$$

including the geometric phase $\gamma = \phi_{\mathrm{I}}$ and a time-dependent dynamic phase ωt. Note that in the last equation, we have neglected relative phase shifts between path I and II at the beam splitter (first plate of the IFM) because they can be adjusted reliably with a phase shifter plate inducing a phase factor $e^{i\chi}$ (see Sec. III D for details). In the next step, an experimental strategy to cancel the dynamic phase component, by use of a second rf flipper [29], is utilized: At the last plate of the interferometer, the two subbeams are recombined, followed by an interaction with the second rf field, with half frequency $\omega/2$ denoted as $B^{(1)} = B_{\mathrm{rf}}^{(\omega)} \cos((\omega/2)t + \phi_{\mathrm{II}}) \cdot \hat{\mathbf{y}}$. The value of ϕ_{II} was set to zero during the complete experiment. Therefore the spin-down component (spin-up from path I, which is flipped at the second rf flipper) acquires a phase $\omega/2(t + T)$, which is the same amount but opposite sign of the phase of the spin-up component (path II). The final state is given by

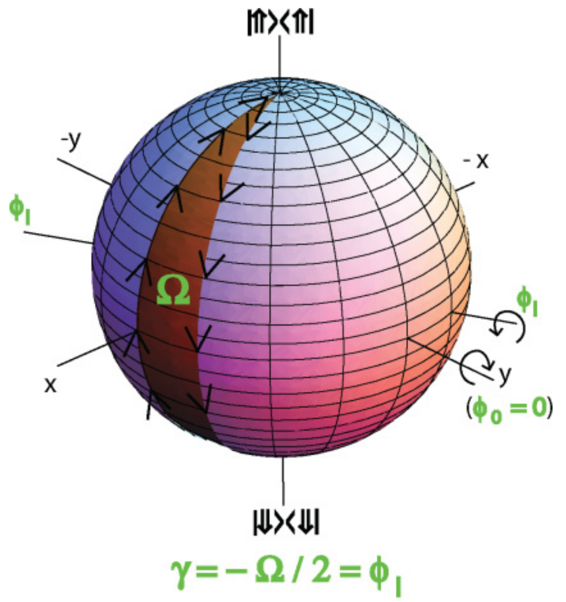

FIG. 2. (Color online) Bloch sphere representation of the spinor evolution within the first rf flipper, placed inside the interferometer (path II), in the rotating frame of reference. The geometric phase γ is given by minus half of the solid angle Ω, traced out by the state vector, depending on the phase ϕ_{I} of the oscillating magnetic field in the rf flipper.

$$\begin{aligned} |\Psi_{\mathrm{Fin}}(\gamma)\rangle = {} & (|\mathrm{I}\rangle + |\mathrm{II}\rangle) \otimes \frac{1}{\sqrt{2}}[e^{i\omega/2(t+T)} e^{i\phi_{\mathrm{II}}}|{\Downarrow}\rangle \\ & + e^{i\chi} e^{i\omega t} e^{-i\omega/2(t+T)} e^{i(\gamma-\phi_{\mathrm{II}})}|{\Uparrow}\rangle] \\ & \propto (|\mathrm{I}\rangle + |\mathrm{II}\rangle) \otimes \frac{1}{\sqrt{2}}[e^{i\chi} e^{i(\gamma-\omega T)}|{\Uparrow}\rangle + |{\Downarrow}\rangle], \end{aligned} \tag{20}$$

where ωT is the zero-field phase, with T being the neutron's propagation time between the two rf flippers and the geometric phase $\gamma = \phi_{\mathrm{I}}$. The instants when the neutron is at the center of the first and second flipper coil are denoted as t and $t + T$, respectively. The energy difference between the orthogonal spin components is compensated by choosing a frequency of $\omega/2$ for the second rf flipper, yielding a stationary state vector (see energy level diagram in Fig. 1).

In our experiment, the $|{\Uparrow}\rangle$ eigenstate (in paths I and II) also acquires a dynamical phase as it precesses about the magnetic guide field in the $+\hat{\mathbf{z}}$ direction. After a spin flip (only in path II), the $|{\Downarrow}\rangle$ eigenstate still gains another dynamical phase but of opposite sign compared to the situation before the spin flip. The phases of the two guide fields and the zero-field phase ωT are compensated by an additional Larmor precession within a tunable accelerator coil with a static field, pointing in the $+\hat{\mathbf{z}}$ direction.

An alternative approach toward the generation of the geometric phase is introduced in Sec. IV, where two rf flippers, one inside and one outside of the interferometer, contribute to the geometric phase.

C. Joint measurements

Experimentally, the probabilities of joint (projective) measurements are proportional to the following count rates, detected after path ($\boldsymbol{\alpha}$) and spin ($\boldsymbol{\beta}$) manipulation:

$$\begin{aligned} N_{++}(\boldsymbol{\alpha},\boldsymbol{\beta}) &= N_{++}[\boldsymbol{\alpha},(\beta_1,0)] \propto \langle\Psi_{\mathrm{Exp}}(\gamma)|\hat{P}^{\mathrm{p}}_{+}(\boldsymbol{\alpha}) \\ &\quad \otimes \hat{P}^{\mathrm{s}}_{+}(\beta_1,0)|\Psi_{\mathrm{Exp}}(\gamma)\rangle, \\ N_{+-}(\boldsymbol{\alpha},\boldsymbol{\beta}) &= N_{++}[\boldsymbol{\alpha},(\beta_1+\pi,0)] \equiv N_{++}[\boldsymbol{\alpha},(\beta_1^{\perp},0)] \\ &\quad \propto \langle\Psi_{\mathrm{Exp}}(\gamma)|\hat{P}^{\mathrm{p}}_{+}(\boldsymbol{\alpha}) \otimes \hat{P}^{\mathrm{s}}_{+}(\beta_1^{\perp},0)|\Psi_{\mathrm{Exp}}(\gamma)\rangle, \\ N_{-+}(\boldsymbol{\alpha},\boldsymbol{\beta}) &= N_{++}[(\alpha_1+\pi,\alpha_2),(\beta_1,0)] \\ &\equiv N_{++}[(\alpha_1^{\perp},\alpha_2),(\beta_1,0)] \propto \langle\Psi_{\mathrm{Exp}}(\gamma)|\hat{P}^{\mathrm{p}}_{+}(\alpha_1^{\perp},\alpha_2) \\ &\quad \otimes \hat{P}^{\mathrm{s}}_{+}(\beta_1,0)|\Psi_{\mathrm{Exp}}(\gamma)\rangle, \\ N_{--}(\boldsymbol{\alpha},\boldsymbol{\beta}) &= N_{++}[(\alpha_1^{\perp},\alpha_2),(\beta_1^{\perp},0)] \propto \langle\Psi_{\mathrm{Exp}}(\gamma)|\hat{P}^{\mathrm{p}}_{+}(\alpha_1^{\perp},\alpha_2) \\ &\quad \otimes \hat{P}^{\mathrm{s}}_{+}(\beta_1^{\perp},0)|\Psi_{\mathrm{Exp}}(\gamma)\rangle. \end{aligned} \tag{21}$$

The expectation value of a joint measurement of $A^{\mathrm{p}}(\boldsymbol{\alpha})$ and $B^{\mathrm{s}}(\boldsymbol{\beta})$,

$$E(\boldsymbol{\alpha},\boldsymbol{\beta}) = \langle\Psi(\gamma)|A^{\mathrm{p}}(\boldsymbol{\alpha}) \otimes B^{\mathrm{s}}(\boldsymbol{\beta})|\Psi(\gamma)\rangle, \tag{22}$$

is experimentally determined from the count rates

$$\begin{aligned} &E(\boldsymbol{\alpha},\boldsymbol{\beta}) \\ &= \frac{N_{++}(\boldsymbol{\alpha},\boldsymbol{\beta}) - N_{+-}(\boldsymbol{\alpha},\boldsymbol{\beta}) - N_{-+}(\boldsymbol{\alpha},\boldsymbol{\beta}) + N_{--}(\boldsymbol{\alpha},\boldsymbol{\beta})}{N_{++}(\boldsymbol{\alpha},\boldsymbol{\beta}) + N_{+-}(\boldsymbol{\alpha},\boldsymbol{\beta}) + N_{-+}(\boldsymbol{\alpha},\boldsymbol{\beta}) + N_{--}(\boldsymbol{\alpha},\boldsymbol{\beta})}. \end{aligned} \tag{23}$$

With these expectation values, S is defined by

$$S = E(\boldsymbol{\alpha},\boldsymbol{\beta}) - E(\boldsymbol{\alpha},\boldsymbol{\beta}') + E(\boldsymbol{\alpha}',\boldsymbol{\beta}) + E(\boldsymbol{\alpha}',\boldsymbol{\beta}'). \tag{24}$$

D. Experimental setup

The experiment was carried out at the neutron interferometer instrument S18 at the high-flux reactor of the Institute Laue-Langevin in Grenoble, France. A sketch of the setup is depicted in Fig. 1. A monochromatic beam with mean wavelength $\lambda_0 = 1.91$ Å$(\Delta\lambda/\lambda_0 \sim 0.02)$ and 5×5 mm^2 beam cross section is polarized by a birefringent magnetic field prism in the $\hat{\mathbf{z}}$ direction [56]. Owing to the angular separation at the deflection, the interferometer is adjusted so that only the spin-up component fulfills the Bragg condition at the first interferometer plate (beam splitter).

As in our previous experiment [29], the spin in path $|\mathrm{II}\rangle$ is flipped by a rf flipper, which requires two magnetic fields: a static field $B_0 \cdot \hat{\mathbf{z}}$ and a perpendicular oscillating field $B^{(1)} = B_{\mathrm{rf}}^{(\omega)} \cos(\omega t + \phi_{\mathrm{I}}) \cdot \hat{\mathbf{y}}$ with amplitude

$$B_{\mathrm{rf}}^{(\omega)} = \frac{\pi\hbar}{\tau|\mu|}, \quad \omega = \frac{2|\mu|B_0}{\hbar}\left(1 + \frac{B_1^2}{16B_0^2}\right), \tag{25}$$

where μ is the magnetic moment of the neutron and τ denotes the time the neutron is exposed to the rf field. The second term in ω is due to the Bloch-Siegert shift [57]. The oscillating field is produced by a water-cooled rf coil with a length of 2 cm, operating at a frequency of $\omega/2\pi = 58$ kHz. The static field is provided by a uniform magnetic guide field $B_0^{(\omega)} \sim 2$ mT, produced by a pair of water-cooled Helmholtz coils.

The two subbeams are recombined at the third crystal plate where $|\mathrm{I}\rangle$ and $|\mathrm{II}\rangle$ only differ by an adjustable phase factor $e^{i\chi}$ (path phase χ is given by $\chi = -Nb_c\lambda D$, with the thickness of the phase shifter plate D, the neutron wavelength λ, the coherent scattering length b_c, and the particle density N in the phase shifter plate). By rotating the plate, χ can be varied systematically. This yields the well-known intensity oscillations of the two beams emerging behind the interferometer.

The O-beam passes the second rf flipper, operating at $\omega/2\pi = 29$ kHz, which is half the frequency of the first rf flipper. The oscillating field is denoted as $B_{\mathrm{rf}}^{(\omega/2)} \cos((\omega/2)t + \phi_{\mathrm{II}}) \cdot \hat{\mathbf{y}}$, and the strength of the guide field was tuned to $B_0^{(\omega/2)} \sim 1$ mT in order to satisfy the frequency resonance condition. This flipper compensates the energy difference between the two spin components by absorption and emission of photons of energy $E = \hbar\omega/2$ (see [29]).

Finally, the spin is rotated by an angle δ (in the $\hat{\mathbf{x}},\hat{\mathbf{z}}$ plane) with a static field spin turner and is analyzed due to the spin-dependent reflection within a Co-Ti multilayer supermirror along the $\hat{\mathbf{z}}$ direction. With this arrangement, consisting of a dc spin turner and a supermirror, the spin can be analyzed along arbitrary directions in the $\hat{\mathbf{x}},\hat{\mathbf{z}}$ plane, determined by δ, which is measured from the $\hat{\mathbf{z}}$ axis [see Fig. 1 and later Fig. 3 (front) for intensity modulations due to χ scans].

E. Experimental strategy

1. *Polar angle adjustment*

Projective measurements are performed on parallel planes defined by $\alpha_2 = \alpha_2' = \beta_2 = \beta_2' = 0$ (see Fig. 1). For the path measurement, the directions are given by $\boldsymbol{\alpha} : \alpha_1 = 0,\ \alpha_2 = 0$ (Fig. 4) and $\boldsymbol{\alpha}' : \alpha_1' = \pi/2,\ \alpha_2' = 0$ (Fig. 3).

The angle $\boldsymbol{\alpha}$, which corresponds to $+\hat{\mathbf{z}}$ (and $-\hat{\mathbf{z}}$ for $\alpha_1^{\perp} = \alpha_1 + \pi = \pi,\ \alpha_2 = 0$), is achieved by the use of a beam block which is inserted to stop beam II (I) in order to measure along $+\hat{\mathbf{z}}$ (and $-\hat{\mathbf{z}}$). The corresponding operators are given by

$$\begin{aligned} \hat{P}^{\mathrm{p}}_{+z}(\alpha_1 = 0,\ \alpha_2 = 0) &= |\mathrm{I}\rangle\langle\mathrm{I}|, \\ \hat{P}^{\mathrm{p}}_{-z}(\alpha_1^{\perp} = \pi,\ \alpha_2 = 0) &= |\mathrm{II}\rangle\langle\mathrm{II}|. \end{aligned} \tag{26}$$

The results of the projective measurement are plotted versus different angles δ of the spin analysis, which is depicted in Fig. 4. Complementary oscillations were obtained because of the spin flip in path $|\mathrm{II}\rangle$. These curves are insensitive to the geometric phase γ because of the lack of superposition with a referential subbeam.

The angle $\boldsymbol{\alpha}'$ is set by a superposition of equal portions of $|\mathrm{I}\rangle$ and $|\mathrm{II}\rangle$, represented on the equator of the Bloch sphere. The interferograms are achieved by a rotation of the phase shifter plate associated with a variation of the path phase χ, repeated at different values of the spin analysis direction δ. The projective measurement for $\alpha_1' = \pi/2, \alpha_2' = 0$ corresponds to a phase shifter position of $\chi = 0$ (and $\alpha_1'^{\perp} = \alpha_1' + \pi = 3\pi/2, \alpha_2' = 0$ to $\chi = \pi$). Projection operators read as

$$\begin{aligned} \hat{P}^{\mathrm{p}}_{+x}\left(\alpha_1' = \frac{\pi}{2}, \alpha_2' = 0\right) &= \frac{1}{2}[(|\mathrm{I}\rangle + |\mathrm{II}\rangle)(\langle\mathrm{I}| + \langle\mathrm{II}|)], \\ \hat{P}^{\mathrm{p}}_{-x}\left(\alpha_1'^{\perp} = \frac{3\pi}{2}, \alpha_2' = 0\right) &= \frac{1}{2}[(|\mathrm{I}\rangle - |\mathrm{II}\rangle)(\langle\mathrm{I}| - \langle\mathrm{II}|)]. \end{aligned} \tag{27}$$

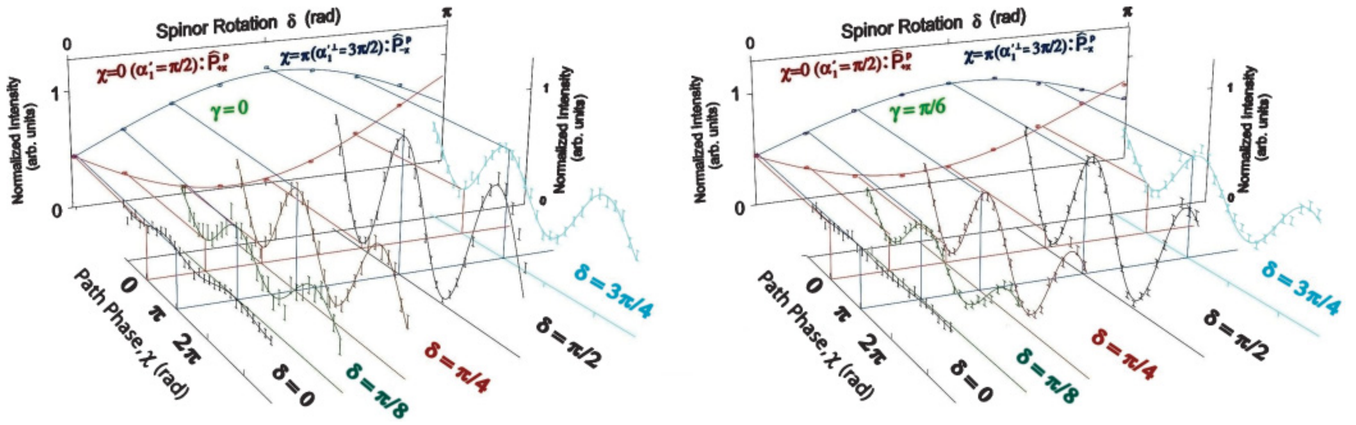

FIG. 3. (Color online) Typical interference patterns of the O-beam ($\alpha_1' = \pi/2$) for $\delta = 0$, $\pi/8$, $\pi/4$, $\pi/2$, $3\pi/4$, being the direction of the spin analysis, and geometric phase (left) $\gamma = 0$ and (right) $\gamma = \pi/6$. Intensities at the path phase $\chi = 0$ and $\chi = \pi$ are extracted from least square fits of the oscillations. (rear) The resulting curves represent the projections to the $\pm\hat{\mathbf{x}}$ direction of the path subspace, denoted as $\hat{P}^{\mathrm{p}}_{+x}$: ($\alpha_1' = \pi/2$, $\alpha_2' = 0$) and $\hat{P}^{\mathrm{p}}_{-x}$: ($\alpha_1'^{\perp} = 3\pi/2$, $\alpha_2' = 0$). The shift of the oscillations (see, e.g., $\delta = \pi/2$) because of the geometric phase γ yields a lower contrast of the curves $\hat{P}^{\mathrm{p}}_{+x}$ and $\hat{P}^{\mathrm{p}}_{-x}$.

The interferogram obtained for $\gamma = 0$ and $\delta = \pi/2$ (Fig. 3) is utilized to determine the zero point of the path phase χ, which defines the $+\hat{\mathbf{x}}$ direction ($\alpha_1' = \pi/2$, $\alpha_2' = 0$) for the path measurement.

In order to obtain phase-shifter scans of higher accuracy, scans over two periods were recorded (see Fig. 3), and the values for $\chi = 0$ and π are extracted from the data by least square fits. These extracted points, marking the $\pm\hat{\mathbf{x}}$ direction of the path measurement, are plotted versus different angles of δ, as shown in Fig. 3 (rear).

All phase-shifter scans were repeated for different angles δ for the spin analysis from $\delta = 0$ to $\delta = \pi$ in steps of $\pi/8$, and for several geometric phases γ (steps of $\pi/6$, and beginning from $\gamma = \pi$, steps of $\pi/4$), as depicted in Fig. 3 (rear) for five selected settings of δ ($\delta = 0,\pi/8,\pi/4,\pi/2,3\pi/4$) and two geometric phases ($\gamma = 0,\pi/6$).

2. Azimuthal angle adjustment

Here the Bell angles (polar angles) remain fixed at the usual values and are set at δ for the projective spin measurement and by the beam block (and fixed phase shifter positions) for the path measurement. The angle between the measurement planes is adjusted by one azimuthal angle (α_2'), which is deduced by phase-shifter (χ) scans.

For the spin measurement, the directions are fixed and given by $\boldsymbol{\beta}$: $\beta_1 = \pi/4$, $\beta_2 = 0$ and $\boldsymbol{\beta}'$: $\beta_1' = 3\pi/4$, $\beta_2' = 0$ (together with $\beta_1^{\perp} = -3\pi/4$, $\beta_1'^{\perp} = -\pi/4$; see Fig. 1 for a Bloch description and Fig. 5 for measured interference patterns). For the projective path measurement, the fixed directions read as $\alpha_1 = 0$ ($\alpha_1^{\perp} = \pi$; see Fig. 4 for measurements with beam block) and $\alpha_1' = \pi/2$ ($\alpha_1'^{\perp} = 3\pi/2$). Phase-shifter ($\chi$) scans

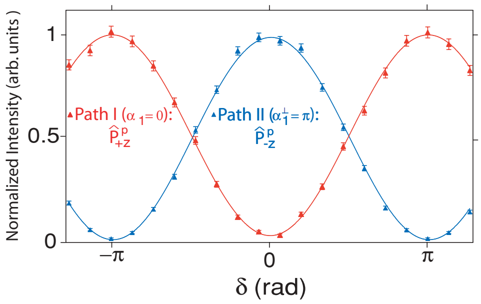

FIG. 4. (Color online) Typical intensity modulations obtained by inserting a beam block, being the projections on the $\pm\hat{\mathbf{z}}$ direction of the path measurement, denoted as $\hat{P}^{\mathrm{p}}_{+z}$: ($\alpha_1 = 0$,$\alpha_2 = 0$) and $\hat{P}^{\mathrm{p}}_{-z}$: ($\alpha_1^{\perp} = \pi$,$\alpha_2 = 0$). The oscillations remain the same when altering the geometric phase.

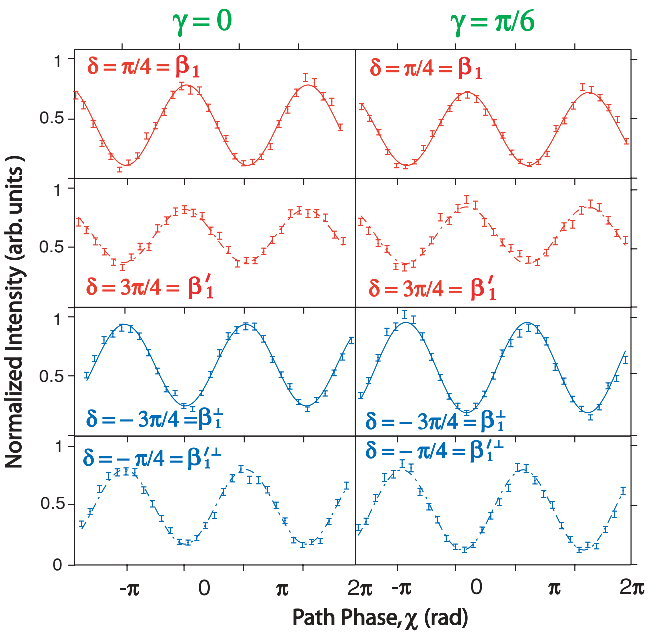

FIG. 5. (Color online) Typical interference patterns of the O-beam ($\alpha_1' = \pi/2$) for $\delta = \pi/4 = \beta_1$, $\delta = 3\pi/4 = \beta_1'$, $\delta = -3\pi/4 = \beta_1^{\perp}$, and $\delta = -\pi/4 = \beta_1'^{\perp}$ ($\beta_2 = \beta_2' = 0$) and geometric phase (left) $\gamma = 0$ and (right) $\gamma = \pi/6$. Phase shifter scans χ are performed for a forthcoming determination of α_2'.

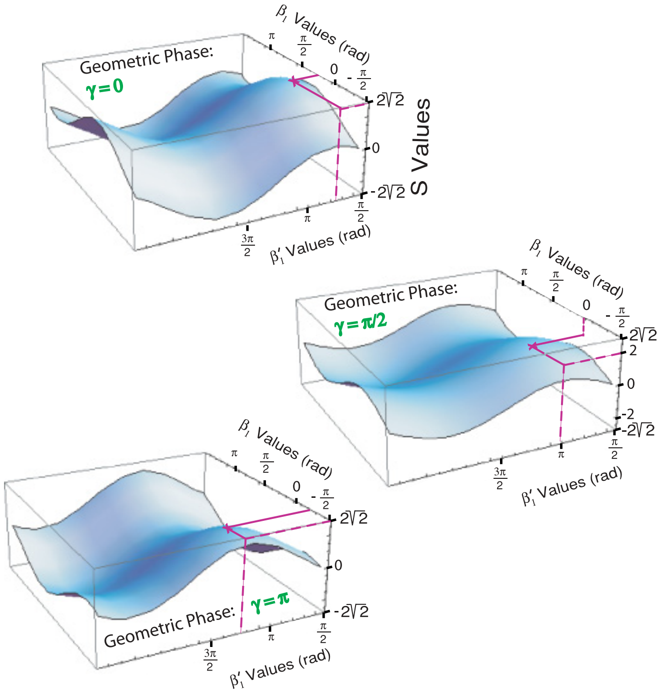

FIG. 6. (Color online) S values for different settings of geometric phases γ, derived from the least square fits of the projective measurements along $\pm\hat{\mathbf{z}}$ (beam block, Fig. 4) and $\pm\hat{\mathbf{x}}$ (varying χ, Fig. 3) directions for the path measurement ($\alpha_1 = 0$, $\alpha_1' = \pi/2$, and $\alpha_2 = \alpha_2' = 0$) using Eq. (11); β_1 and β_1' represent the directions of the spin analysis, which are changed systematically by a variation of δ, while β_2 and β_2' remain constant at the value zero (polar adjustment). The position of the maximum is determined numerically for different settings of the geometric phases γ (here, e.g., $\gamma = 0$ where $S_{\mathrm{MAX}} = 2\sqrt{2}$, $\gamma = \pi/2$ with $S_{\mathrm{MAX}} = 2$, and $\gamma = \pi$ with $S_{\mathrm{MAX}} = 2\sqrt{2}$). The β_1 and β_1' values result, as predicted, in Eqs. (13a) and (13b) for S_{MAX}.

are performed in order to determine α_2', which is depicted in Fig. 5 for two values of the geometric phase: $\gamma = 0$ and $\gamma = \pi/6$. One can see a shift of the oscillations due to the geometric phase γ.

F. Data analysis and experimental results

1. *Polar angle adjustment*

Using least square fits from the polar angle adjustment measurement curves in Figs. 3 and 4, together with Eq. (24), the S value is calculated as a function of the parameters β_1 and β_1' which are plotted in Fig. 6 for $\gamma = 0$, $\gamma = \pi/2$, and $\gamma = \pi$ ($\gamma = 0$ and $\gamma = \pi$ are chosen since the fringe displacement is maximal for these two settings and $\gamma = \pi/2$ illustrates the increase of S to a value of 2). The local maximum of the surface is determined numerically. The settings for β_1 and β_1', yielding a maximal S value, are compared with the predicted values for β_1 and β_1' from Eqs. (13a) and (13b), respectively.

The resulting S values, derived using the adjusted Bell angles β_1 and β_1', are plotted in Fig. 7(a) versus the geometric phase γ. The theoretical predictions from Eq. (11) depicted as a solid green line are evidently reproduced. The maximal S decreases from $\gamma = 0$ to $\gamma = \pi/2$, where the boundary of the CHSH inequality $S = 2$ is reached, followed by an increase to the familiar value $S = 2\sqrt{2}$.

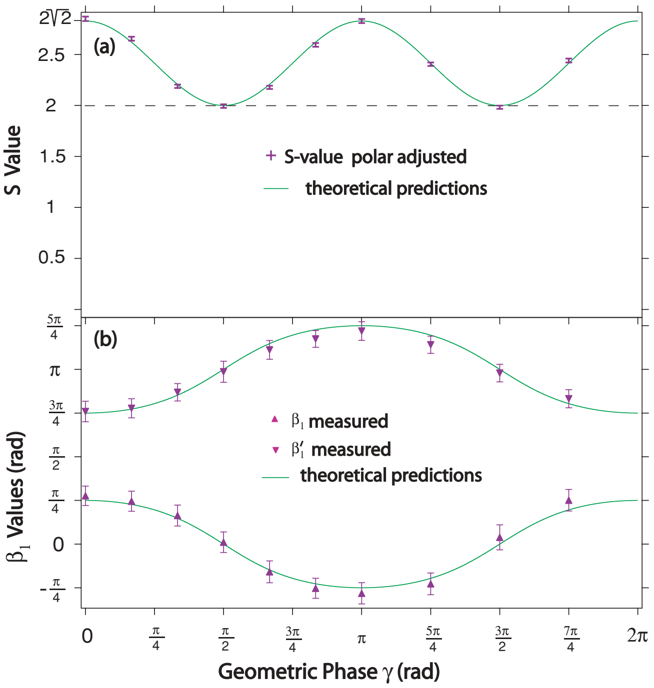

FIG. 7. (Color online) (a) Polar-adjusted S values vs. geometric phase γ with adapted Bell angles (β_1 and β_1') according to the geometric phase γ. (b) Corresponding modified Bell angles plotted vs. the geometric phase γ.

In Fig. 7(b), the deduced β_1 and β_1' values are plotted versus the geometric phase γ; β_1 and β_1' follow the theoretical behavior (solid green line) predicted by Eqs. (13a) and (13b). One can see a peak for β_1 (and a dip for β_1') at $\gamma = \pi$.

2. *Azimuthal angle adjustment*

In Fig. 8 we depict selected S values calculated from least square fits of the azimuthal angle adjustment measurements, where $\beta_1 = \pi/4$, $\beta_1' = 3\pi/4$, $\beta_1^{\perp} = 5\pi/4$, $\beta_1'^{\perp} = -\pi/4$, and $\alpha_1' = \pi/2$ (see Fig. 5) and $\alpha_1 = 0$, $\alpha_1^{\perp} = \pi$ (Fig. 4) versus geometric phase γ. A simple shift of the oscillation of the S value is observed because of the geometric phase [see Fig. 8 (front)]. The maximum S value of $2\sqrt{2}$ is always found for $\alpha_2' = \gamma$, which is indicated in Fig. 8 (rear). The complete measurement set of S values versus the geometric phase γ is plotted in Fig. 9(a) (S value azimuthal adjusted). If no adjustment is applied to α_2, which means α_2' is always kept constant at $\alpha_2 = 0$, S approaches zero at $\gamma = \pi$ and returns to the maximum value $2\sqrt{2}$ at $\gamma = 2\pi$ [see Fig. 9(a), S value without adjustment].

Figure 9(b) shows adjusted α_2' versus the geometric phase γ: It is clearly seen that adjusted α_2' fulfills the theory condition (solid green line), namely, a linear dependency as expressed in Eq. (15a).

IV. DISCUSSION

If no corrections are applied to the Bell angles, the S value decreases from $2\sqrt{2}$ at $\gamma = 0$ to zero at $\gamma = \pi$ and

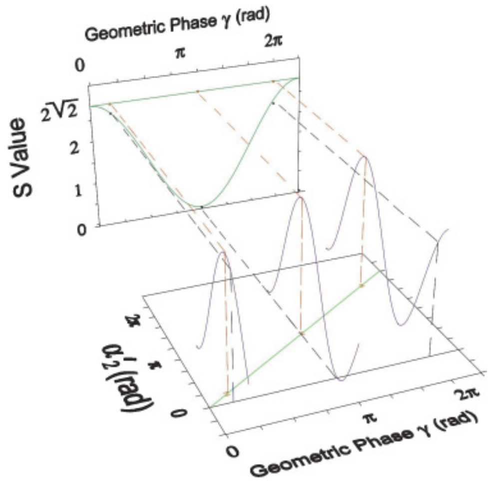

FIG. 8. (Color online) S values derived from least square fits of the projective spin and path measurements for $\beta_1 = \pi/4$, $\beta_1' = 3\pi/4$, $\beta_1^{\perp} = -3\pi/4$, $\beta_1'^{\perp} = -\pi/4$, and $\alpha_1' = \pi/2, \alpha_1'^{\perp} = 3\pi/2$ (see Fig. 5) and $\alpha_1 = 0, \alpha_1^{\perp} = \pi$ (see Fig. 4) vs. geometric phase γ. The maximum S value of $2\sqrt{2}$ is always found for $\alpha_2' = \gamma$, as predicted in Eq. (15a) (azimuthal adjustment). If no corrections are applied to the Bell angles ($\alpha_2' = 0$), S approaches zero at $\gamma = \pi$.

regains the value of $2\sqrt{2}$ at $\gamma = 2\pi$ [Fig. 9(a), S value without adjustment]. Keeping the azimuthal angles fixed, an appropriate adjustment of the polar Bell angles determined by the geometric phase [$\beta_1 = \arctan(\cos\gamma)$] yields a sinusoidal oscillation of the S value [$2 \leqslant S \leqslant 2\sqrt{2}$, with period π; see Fig. 7(a)]. Finally, the maximum S value of $2\sqrt{2}$ can be observed for all values of the geometric phase γ if the difference of the azimuthal angles (angle between the analysis planes) equals the geometric phase ($\alpha_2' = \gamma$), while the polar Bell angles remain unchanged at typical values for testing of a Bell inequality [Fig. 9(a), S value azimuthal adjusted].

Owing to the inherent phase instability of the neutron interferometer, it is necessary to perform a reference measurement for each setting of γ and δ. This is achieved by turning off the rf flipper inside the interferometer, yielding a reference interferogram. The oscillations plotted in Figs. 3 and 5 are normalized by the contrast of the reference measurement.

At this point it should be noted that the average contrast of ~50% (obtained for $\delta = \pi/2$ with maximum intensity of ~25 neutrons/s) is below the threshold of 70.7% required to observe a violation of a Bell inequality. Violation of a Bell-like inequality for a spin-path entanglement in neutron interferometry has already been reported in [16]; the argument in this article is the influence of the geometric phase on the S value. Consequently, a normalization as performed does not influence the validity of the results presented here.

Next we want to discuss some systematic errors in our experiment, in particular, in the state preparation and in the projective spin measurement. Under ideal conditions, no interference fringes should be obtained in the H beam because of the orthogonal spin states in the interfering subbeams. Nevertheless, we have observed intensity modulations with a contrast of a few percent. This indicates that the state preparation (rf flipper) was not perfect in some sense. The expectation values for the joint measurements [Eqs. (7)–(11)] can be deduced for an arbitrary (spin) state in the path of the IFM where the rf flipper is located:

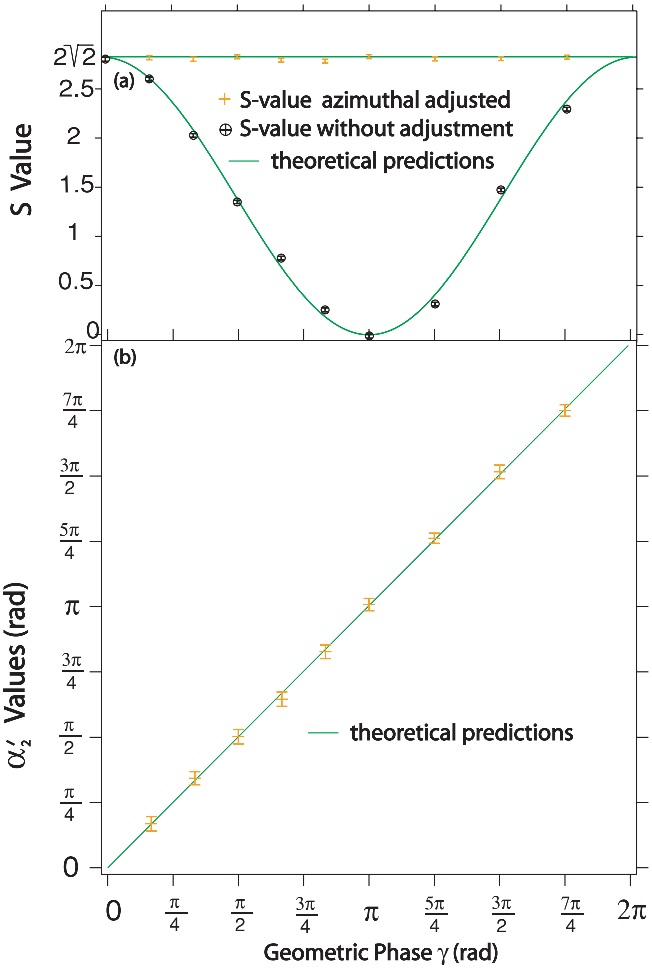

FIG. 9. (Color online) (a) Azimuthal-adjusted S values vs. geometric phase γ with balanced Bell angle (α_2') according to the geometric phase γ and without corrections. (b) Corresponding modified Bell angle plotted vs. the geometric phase γ.

$$|\Psi_{\text{Meas.}}(\gamma)\rangle = \frac{1}{\sqrt{2}}\left[|\text{I}\rangle \otimes |\Uparrow\rangle + e^{i\chi}|\text{II}\rangle \otimes e^{i\gamma}\left(\sin\frac{\theta}{2}|\Uparrow\rangle + e^{i\omega t}\cos\frac{\theta}{2}|\Downarrow\rangle\right)\right]. \tag{28}$$

Here θ is determined by the fringe contrast in the H beam. These systematic deviations from the theoretical initial state have been taken into account in the calculation of the final S value.

The asymmetry in the curve of the projective measurement along the $\pm\hat{\mathbf{x}}$ direction of the path measurement, denoted as $\hat{P}^{\text{p}}_{+x} : (\alpha_1' = \pi/2, \alpha_2' = 0)$ and $\hat{P}^{\text{p}}_{-x} : (\alpha_1'^{\perp} = 3\pi/2, \alpha_2' = 0)$ in Fig. 3, is considered to result from a misalignment of the static magnetic fields at the position of the coil such as the stray field of the first guide field, the second guide field, and the two fields in the $(\hat{\mathbf{x}},\hat{\mathbf{z}})$ direction produced by the coil itself.

At this point we want to introduce an alternative approach toward the generation of geometric phase, where unlike in the proposed setup in [48], the geometric phase is not acquired solely in one arm of the interferometer. Here the two rf

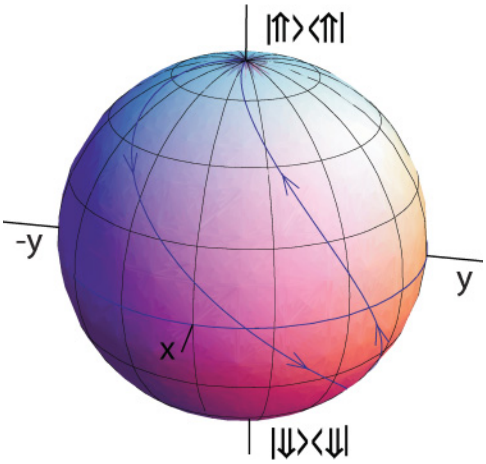

FIG. 10. (Color online) Bloch sphere representation of the spinor evolution within the first rf flipper (frequency ω, $\phi_{\mathrm{I}} = \pi/2$) placed inside the interferometer (path II) and second rf flipper (frequency $\omega/2$, $\phi_{\mathrm{II}} = 0$). The geometric phase γ is given by minus half of the solid angle Ω, traced out by the state vector.

flippers, one inside and one outside of the interferometer, contribute to the geometric phase generation, while dynamic phases accumulated in the two curves are canceled [58,59]. (For simplicity, we assume here two rf flippers in the same length.) From the laboratory frame, the spinor evolution within the rf flipper placed inside the interferometer (path II) and the second rf flipper is the following: The neutron spin traces out a curve from $|\Uparrow\rangle$ to $|\Downarrow\rangle$ on the Bloch sphere, whose polar and azimuthal angles increase linearly with time at the rates ω. The spin returns to its initial state $|\Uparrow\rangle$ when passing the second rf flipper operating at a frequency of $\omega/2$. The $|\Uparrow\rangle$-to-$|\Downarrow\rangle$ and $|\Downarrow\rangle$-to-$|\Uparrow\rangle$ curves intersect the equator at the azimuthal angles $\omega t + \phi_{\mathrm{I}} - \pi/2$ and $\omega(t+T)/2 + \phi_{\mathrm{II}} + \pi/2$, respectively, which can be seen in Fig. 10. The solid angle Ω yields a pure geometric phase $\gamma = -\Omega/2$, as in [60,61]. The geometric phase γ acquired on path II is given by

$$\begin{aligned} \gamma = -\Omega/2 &= \omega t - \omega/2(t+T) + \phi_{\mathrm{I}} - \phi_{\mathrm{II}} - \pi \\ &= \omega(t-T)/2 + \phi_{\mathrm{I}} - \pi \end{aligned} \tag{29}$$

because $\phi_{\mathrm{II}} = 0$, with t and $t+T$ denoting the instants when the neutron is at the center of the first and second flipper coil, respectively. The term π arises from the second spin flip ($|\Downarrow\rangle$-to-$|\Uparrow\rangle$), starting at an azimuthal angle further than the up-to-down curve by π.

The time-dependent phase is eliminated, as already discussed in Sec. III B; the reference beam (path I) is also exposed to the second rf flipper placed outside the interferometer, operating at frequency $\omega/2$. Therefore the spin-down component (spin-up from path I and flipped at second rf flipper) acquires a phase $\omega/2(t+T)$, which is the same amount but opposite sign of the spin-up component (path II). Consequently, the time dependence of the phase is compensated by choosing a frequency of $\omega/2$ for the second rf flipper. This results in observation of a time-independent phase with the only variable part being ϕ_{I} (the remaining terms are given by π and ωT, with T being the neutrons' propagation time between the two rf flippers [62]).

V. CONCLUSION

We have demonstrated a technique to balance the influence of the geometric phase generated by one subspace of the system, considering a Bell-like inequality. This is achieved by an appropriate adjustment of the polar Bell angles (keeping the measurement planes fixed) or one azimuthal angle (keeping the polar Bell angles at the well-known values), determined by a laborious measurement procedure. It is demonstrated, in particular, that a geometric phase in one subspace does not lead to a loss of entanglement, determined by a violation of a Bell-like inequality. The experimental data are in good agrement with theoretical predictions presented in [48], demonstrating the correctness of the procedure as a matter of principle.

ACKNOWLEDGMENTS

We thank E. Balcar for a critical reading of the article. This work has been supported by the Austrian Science Foundation, FWF (Grant Nos. P21193-N20 and T389-N16).

---

[1] A. Einstein, B. Podolsky, and N. Rosen, Phys. Rev. **47**, 777 (1935).
[2] E. Schrödinger, Naturwissenschaften **23**, 807 (1935); **23**, 823 (1935); **23**, 844 (1935).
[3] J. S. Bell, Physics (NY) **1**, 195 (1964).
[4] J. S. Bell, *Speakable and Unspeakable in Quantum Mechanics* (Cambridge University Press, Cambridge, 1987).
[5] J. F. Clauser, M. A. Horne, A. Shimony, and R. A. Holt, Phys. Rev. Lett. **23**, 880 (1969).
[6] R. A. Bertlmann and A. Zeilinger, *Quantum [Un]speakables, from Bell to Quantum Information* (Springer, Heidelberg, 2002).
[7] S. J. Freedman and J. F. Clauser, Phys. Rev. Lett. **28**, 938 (1972).
[8] A. Aspect, P. Grangier, and G. Roger, Phys. Rev. Lett. **47**, 460 (1981).
[9] P. G. Kwiat, K. Mattle, H. Weinfurter, A. Zeilinger, A. V. Sergienko, and Y. Shih, Phys. Rev. Lett. **75**, 4337 (1995).
[10] G. Weihs, T. Jennewein, C. Simon, H. Weinfurter, and A. Zeilinger, Phys. Rev. Lett. **81**, 5039 (1998).
[11] W. Tittel, J. Brendel, H. Zbinden, and N. Gisin, Phys. Rev. Lett. **81**, 3563 (1998).
[12] M. A. Rowe, D. Kielpinski, V. Meyer, C. A. Sackett, W. Itano, C. Monroe, and D. J. Wineland, Nature (London) **409**, 791 (2001).
[13] D. L. Moehring, M. J. Madsen, B. B. Blinov, and C. Monroe, Phys. Rev. Lett. **93**, 090410 (2004).
[14] H. Sakai *et al.*, Phys. Rev. Lett. **97**, 150405 (2006).
[15] D. N. Matsukevich, P. Maunz, D. L. Moehring, S. Olmschenk, and C. Monroe, Phys. Rev. Lett. **100**, 150404 (2008).

[16] Y. Hasegawa, R. Loidl, G. Badurek, M. Baron, and H. Rauch, Nature (London) **425**, 45 (2003).

[17] J. S. Bell, Rev. Mod. Phys. **38**, 447 (1966).

[18] N. D. Mermin, Rev. Mod. Phys. **65**, 803 (1993).

[19] C. Simon, M. Żukowski, H. Weinfurter, and A. Zeilinger, Phys. Rev. Lett. **85**, 1783 (2000).

[20] S. Kochen and E. P. Specker, J. Math. Mech. **17**, 59 (1967).

[21] A. Cabello, Phys. Rev. Lett. **101**, 210401 (2008).

[22] A. Cabello, S. Filipp, H. Rauch, and Y. Hasegawa, Phys. Rev. Lett. **100**, 130404 (2008).

[23] G. Kirchmair, F. Zahringer, R. Gerritsma, M. Kleinmann, O. Guhne, A. Cabello, R. Blatt, and C. F. Roos, Nature (London) **460**, 494 (2009).

[24] Y. Hasegawa, R. Loidl, G. Badurek, M. Baron, and H. Rauch, Phys. Rev. Lett. **97**, 230401 (2006).

[25] H. Bartosik, J. Klepp, C. Schmitzer, S. Sponar, A. Cabello, H. Rauch, and Y. Hasegawa, Phys. Rev. Lett. **103**, 040403 (2009).

[26] H. Rauch, W. Treimer, and U. Bonse, Phys. Lett. A **47**, 369 (1974).

[27] H. Rauch and S. A. Werner, *Neutron Interferometry* (Clarendon Press, Oxford, 2000).

[28] Y. Hasegawa, R. Loidl, G. Badurek, S. Filipp, J. Klepp, and H. Rauch, Phys. Rev. A **76**, 052108 (2007).

[29] S. Sponar, J. Klepp, R. Loidl, S. Filipp, G. Badurek, Y. Hasegawa, and H. Rauch, Phys. Rev. A **78**, 061604(R) (2008).

[30] M. V. Berry, Proc. R. Soc. London A **392**, 45 (1984).

[31] A. Tomita and R. Y. Chiao, Phys. Rev. Lett. **57**, 937 (1986).

[32] T. Bitter and D. Dubbers, Phys. Rev. Lett. **59**, 251 (1987).

[33] Y. Aharonov and J. Anandan, Phys. Rev. Lett. **58**, 1593 (1987).

[34] J. Samuel and R. Bhandari, Phys. Rev. Lett. **60**, 2339 (1988).

[35] S. Pancharatnam, Proc. Indian Adac. Sci. A **44**, 247 (1956).

[36] N. Manini and F. Pistolesi, Phys. Rev. Lett. **85**, 3067 (2000).

[37] Y. Hasegawa, R. Loidl, M. Baron, G. Badurek, and H. Rauch, Phys. Rev. Lett. **87**, 070401 (2001).

[38] Y. Hasegawa, R. Loidl, G. Badurek, M. Baron, N. Manini, F. Pistolesi, and H. Rauch, Phys. Rev. A **65**, 052111 (2002).

[39] E. Sjöqvist, A. K. Pati, A. Ekert, J. S. Anandan, M. Ericsson, D. K. L. Oi, and V. Vedral, Phys. Rev. Lett. **85**, 2845 (2000).

[40] S. Filipp and E. Sjöqvist, Phys. Rev. A **68**, 042112 (2003).

[41] S. Filipp and E. Sjöqvist, Phys. Rev. Lett. **90**, 050403 (2003).

[42] J. Klepp, S. Sponar, Y. Hasegawa, E. Jericha, and G. Badurek, Phys. Lett. A **342**, 48 (2005).

[43] J. Klepp, S. Sponar, S. Filipp, M. Lettner, G. Badurek, and Y. Hasegawa, Phys. Rev. Lett. **101**, 150404 (2008).

[44] M. A. Nielsen and I. Chuang, *Quantum Computation and Quantum Information* (Cambridge University Press, Cambridge, 2000).

[45] P. J. Leek, J. M. Fink, A. Blais, R. Bianchetti, M. Göppl, J. M. Gambetta, D. I. Schuster, L. Frunzio, R. J. Schoelkopf, and A. Wallraff, Science **318**, 1889 (2007).

[46] S. Filipp, J. Klepp, Y. Hasegawa, C. Plonka-Spehr, U. Schmidt, P. Geltenbort, and H. Rauch, Phys. Rev. Lett. **102**, 030404 (2009).

[47] E. Sjöqvist, Phys. Rev. A **62**, 022109 (2000).

[48] R. A. Bertlmann, K. Durstberger, Y. Hasegawa, and B. C. Hiesmayr, Phys. Rev. A **69**, 032112 (2004).

[49] D. M. Tong, L. C. Kwek, and C. H. Oh, J. Phys. A **36**, 1149 (2003).

[50] R. Das, S. K. Kumar, and A. Kumar, J. Magn. Reson. **177**, 318 (2005).

[51] S. Basu, S. Bandyopadhyay, G. Kar, and D. Home, Phys. Lett. A **279**, 281 (2001).

[52] R. Gähler and R. Golub, Phys. Lett. A **123**, 43 (1987).

[53] R. Golub, R. Gähler, and T. Keller, Am. J. Phys. **62**, 779 (1994).

[54] S. V. Grigoriev, W. H. Kraan, and M. T. Rekveldt, Phys. Rev. A **69**, 043615 (2004).

[55] D. Suter, K. T. Mueller, and A. Pines, Phys. Rev. Lett. **60**, 1218 (1988).

[56] G. Badurek, R. J. Buchelt, G. Kroupa, M. Baron, and M. Villa, Physica B **283**, 389 (2000).

[57] F. Bloch and A. Siegert, Phys. Rev. **57**, 522 (1940).

[58] S.-L. Zhu and Z. D. Wang, Phys. Rev. A **67**, 022319 (2003).

[59] Y. Ota, Y. Goto, Y. Kondo, and M. Nakahara, Phys. Rev. A **80**, 052311 (2009).

[60] A. G. Wagh, G. Badurek, V. C. Rakhecha, R. J. Buchelt, and A. Schricker, Phys. Lett. A **268**, 209 (2000).

[61] B. E. Allman, H. Kaiser, S. A. Werner, A. G. Wagh, V. C. Rakhecha, and J. Summhammer, Phys. Rev. A **56**, 4420 (1997).

[62] S. Sponar, J. Klepp, G. Badurek, and Y. Hasegawa, Phys. Lett. A **372**, 3153 (2008).